EES Catalysis

PAPER

View Article Online
View Journal | View Issue

Cite this: *EES Catal.*, 2025, 3, 1377

Historical experimental data and theoretical volcano map-accelerated cross-scale design of a highly active and durable ternary alloy electrocatalyst for formic acid oxidation

Pengcheng Liu,†[ab] Dezhi Su,†[b] Xiao Chen,†[b] Yanyi Liu,[b] Kaili Wang,*[c] Da Chen,*[a] Xijun Liu[d] and Jia He*[b]

Received 16th May 2025,
Accepted 29th July 2025

DOI: 10.1039/d5ey00149h

rsc.li/eescatalysis

Traditional studies in comprehensive multicomponent spaces driven by redundant chemical experiments may overlook important features. Herein, we introduce historical experimental data and a theoretical volcano map, coupled with thermodynamic stability, to provide insights by feature ranking based on a robust formic acid oxidation reaction (FOR) database. Results indicate that the PdCuNi alloy catalyst screened by density functional theory (DFT) calculations and machine learning (ML) is a promising candidate for FOR. Electron-deficient surface Ni atoms promote the reduction of the thermodynamic energy barrier of FOR. A PdCuNi medium entropy alloy aerogel (PdCuNi AA) was successfully synthesized through a simple one-pot $NaBH_4$-reduction synthesis strategy. The obtained catalyst exhibits a mass activity of 2.7 A mg^{-1}, surpassing those of PdCu, PdNi and commercial Pd/C by approximately 2.1-, 2.7- and 6.9-fold, respectively. Moreover, PdCuNi AA achieves an impressive power density of around 153 mW cm^{-2} with 0.5 mg cm^{-2} loading in the anode of direct formic acid fuel cells. Combining cutting-edge methods to drive innovative catalyst design will play a key role in advancing the development of fuel cells.

Broader context

Traditional trial-and-error methods in complex multicomponent systems often overlook critical features. Integrating historical data, theoretical volcano maps, and thermodynamic stability *via* feature ranking (using a robust FOR database), the DFT/ML-screened PdCuNi alloy emerges as a superior FOR catalyst. The one-pot-synthesized PdCuNi medium-entropy alloy aerogel achieves 2.7 A mg^{-1} (6.9 × Pd/C) and 153 mW cm^{-2} in DFFCs. This approach accelerates the innovation of fuel cell catalysts.

1. Introduction

Direct formic acid fuel cells (DFFCs), with formic acid as anode fuel, have the advantages of high theoretical open potential (1.48 V), high energy density and low formic acid cross penetration and thus have great potential in the field of portable power generation.[1–6] Previous reports have shown that Pd-based catalysts are well known for their fast theoretical kinetics on FOR.[3,6] Nonetheless, FOR is slow, unstable and limited by low output power, low current density, poor stability, and high manufacturing cost, thus making its commercial scale process subject to constraints. One of the challenges with Pd-based catalysts is controlling the pathway for CO_2 dissociation, which leads to CO being adsorbed and poisoning of the active sites of the catalyst surface, resulting in subsequent reduction of the catalyst activity.[7–9] Various approaches have been developed to

[a] *Tianjin Engineering Research Center of Civil Aviation Energy Environment and Green Development, School of Transportation Science and Engineering, Civil Aviation University of China, Tianjin 300300, China. E-mail: chenda@cauc.edu.cn*
[b] *Tianjin Key Laboratory of Organic Solar Cells and Photochemical Conversion, School of Chemistry and Chemical Engineering and Institute of New Energy Materials & Low-Carbon Technologies, Tianjin University of Technology, Tianjin 300384, China. E-mail: hejia1225@126.com*
[c] *School of Chemistry & Chemical Engineering and Environmental Engineering, Weifang University, Weifang 261061, China. E-mail: wangkaili920823@163.com*
[d] *State Key Laboratory of Featured Metal Materials and Life-cycle Safety for Composite Structures, Guangxi Key Laboratory of Processing for Non-ferrous Metals and Featured Materials, School of Resources, Environment and Materials, Guangxi University, Nanning 530004, Guangxi, China*
† P. C. L., D. Z. S. and X. C. contributed equally to this work.

enhance their catalytic performance. One example is alloying with non-precious metal atoms to adjust their electronic structure by modifying the d-band center of Pd-based catalysts. This is significant for avoiding CO poisoning and enhancing water activation capabilities to improve the catalytic activity by reducing the energy barrier of FOR. Although significant progress has been made in Pd-based catalysts, the pursuit of their structural design and high performance remains a key issue in the current development of DFFCs.[1,6,8,9]

Medium entropy alloy (MEAs) catalysts, consisting of no less than three atoms, offer a flexible platform to adjust their electronic structure due to their diverse multi-components and high dispersion of atomically mixed structures.[4,10] In comparison to traditional single-component metals and two-component alloys, MEAs offer significant advantages encompassing high activity, superior selectivity, remarkable stability, and cost-effectiveness, thereby exhibiting immense potential for clean energy application. Medium entropy amorphous alloys, as a unique alloy material with long-range order and low crystallinity, are new promising and competitive candidates for electrochemical catalysts. This is due to their high density of low-coordination sites, high Gibbs free energy states, expanded electrochemical surface area, and robust corrosion resistance devoid of phase boundaries, which can avoid the limitation of crystallinity, making MEAs free from strict composition restrictions.[11–14] They can be synthesized through various methods, such as chemical reduction of metal precursor salts using BH^{4-} or $H_2PO_3{}^{2-}$, electrodeposition, and ion beam deposition. Wang *et al.*[15] employed a glassy non-noble metal core created through specialized ligand adsorption, and the synthesized PdCu-NWs achieved an impressive specific activity of 5.33 mA cm^{-2} in the HCOOH dehydrogenation reaction. Pei *et al.*[16] developed an electrodeposited amorphous Ni–P alloy, which possesses an exceptionally high energy state that significantly elevates the catalytic performance in the urea oxidation reaction owing to its heterogeneous structure. The modified Ni–P NG (nanostructured metallic glasses) catalyst demands a mere potential of 1.36 V to achieve a higher current density of 10 mA cm^{-2}, accompanied by a remarkable Tafel slope of 13 mV dec^{-1}. Because of these unique characters, alloy aerogel (AA) electrocatalysts have been developed to enhance the efficiency of the oxygen reduction reaction (ORR),[17] methanol oxidation reaction (MOR),[18] and the oxygen evolution reaction (OER).[19]

The rational design of AA electrocatalysts is a great challenge due to the large composition space and abundant surface-active sites. Specifically, significant computational resources are required to reveal the adsorption energy distribution of a single adsorbed intermediate on a surface, unlike metals and alloys that have an ordered structure.[20–23] Currently, DFT research methodologies have offered robust technical underpinnings for this domain.[24] The highly efficient electrocatalysts marry the linear scaling relationship between adsorption energies of diverse intermediates with volcano plots, and leverage low-dimensional descriptors, such as adsorption energy.[23] Rossmeisl *et al.* harnessed volcano plots to illustrate the adsorption free energy of CO* and *OH, effectively screening the methanol oxidation reaction (MOR) activity of diverse binary transition metal alloys to identify alloy catalysts that occupy the vertex of the volcano plot.[25–27] Beyond employing adsorption energy as a descriptor, various electronic structure properties of catalysts, including d-band centers and orbital occupancy numbers of e_g, are commonly utilized in the development of alloy electrocatalysts. For example, Zhou *et al.* introduced p-band descriptors to show that the N-doped graphene heterostructure supported by an MXene monolayer displays exceptional dual-functional activity in ORR and HER. This is attributed to the downward shift of the p-band center of the carbon atom, resulting from the interplay between the p-orbital and the adsorbate.[21,22] Although DFT is known for its in-depth insights into the microscopic properties of materials, it insufficiently explores the mesoscopic and macroscopic properties of materials, leaving significant knowledge gaps. In addition, when faced with complex systems or dynamic electronic systems, DFT may consume a large amount of computing resources and extensive calculation time, limiting its application in large-scale or high-real-time research.[28–33] Therefore, combining DFT with other research methods can efficiently reveal the formation of macroscopic properties of materials, to comprehensively and deeply understand the essential characteristics of materials from microscopic mechanisms to macroscopic performance, which can provide a more solid and comprehensive theoretical basis for the design and application of materials.[34,35]

Machine learning (ML) has been proven as an efficient approach to achieve the accelerated design of cutting-edge novel electrocatalysts.[34–37] Isayev *et al.* utilized the enhanced simplex method to extract the structural features of the material and fuse them with its electronic characteristics to formulate a regression model for prediction, ultimately aiming to discover the material possessing the highest superconducting critical temperature.[35] Ding *et al.*[38] introduced artificial intelligence-assisted models to determine the key parameters of non-precision metal electrocatalysts based on the proton exchange membrane fuel cell (PEMFC), avoiding the necessary experiments in the development process of the membrane electrode assembly (MEA). It offers profound insights into the individual roles played by each element within the quaternary high entropy alloy system.[36,38–45] While ML methods possess remarkable capabilities, they encounter limitations in their application as they predominantly analyze and screen the macroscopic properties of known catalysts, often overlooking the nuanced features of materials at the microscopic level. Consequently, to delve deeper into the unexplored realm of FOR catalysts, it is equally crucial to harness the power of ML technology for comprehensive exploration.[35,36]

Therefore, we developed a hybrid-driven design scheme based on DFT, ML and experimental approaches to design an intelligent AA electrocatalyst for high performance DFFCs. At first, multi-component metal-based electrocatalysts were rigorously screened on the adsorption free energy of intermediates *CO and *OH by constructing over 300 computational models based on DFT methods, and the underlying factors

contributing to their superior FOR reactivity were thoroughly investigated. DFT results show that the PdCuNi alloy exhibits encouraging FOR performance. Based on the above DFT results, we then curated a robust database encompassing 392 catalysts to capture pivotal structural information, with the mass activity (MA) of FOR serving as the focal learning target. We used multiple methods including decision trees, correlation coefficient heat maps, and feature importance scores to perform mining for the database. Furthermore, we utilized 15 machine learning algorithms to identify ternary alloy catalysts exhibiting superior FOR activity. Random forest regression (RFR) demonstrated outstanding performance on our catalyst database. We utilized RFR to screen 50 000 catalysts generated by the sequence model algorithm configuration (SMAC). Furthermore, the stability was rigorously and comprehensively assessed, with catalysts exhibiting formation energies of less than 0 eV being considered thermodynamically stable, and encompassing diverse alloy catalysts such as PdCuNi, PdCuAg, PdAgAu, and PdAuCu. By integrating ML and DFT, a series of potential FOR mechanisms for PdCuNi were identified, ultimately leading to the determination of the optimal reaction pathway. To reveal the capabilities of the hybrid approach of ML and DFT, PdCuNi AA was successfully synthesized as a controlled experiment.

Attributed to the favorable electronic interplay between Pd, Cu, and Ni, the PdCuNi AA exhibits a remarkable mass activity of 2.7 A mg^{-1} for FOR in an acidic solvent, which is approximately 6–9 times higher than that of commercial Pd/C. Additionally, it achieves a commendable power density of up to 153 mW cm^{-2} in DFFCs. The integration of advanced methodologies of DFT and ML in driving new material design will significantly propel the advancement of electrocatalysis in the DFFCs field.

2. Results and discussion

2.1. Hybrid driving design of FOR electrocatalysts

The framework for the hybrid driving design of new ternary FOR electrocatalysts by combining DFT calculations and high-throughput ML technology is illustrated in Fig. 1(a). A previous study clearly demonstrated that the adsorption free energies of *CO and *OH bound to the surface (G_{*CO} and G_{*OH}) are effective descriptors for the FOR electrocatalysis. The Brønsted–Evans–Polanyi (BEP) relationship, which is based on the adsorption free energy of reaction intermediates, can fully bridge the gap between thermodynamic data and kinetic processes.[46,47] As illustrated in Fig. 1(b) and Table S1, the volcano plot, which is constructed by linearly scaling the adsorption energy of *CO and *OH reaction intermediates, offers valuable mechanistic insights for designing and screening such heterogeneous catalysts. Within the FOR-volcano plot, the adsorption free energies of *CO and *OH intermediates emerge as the pivotal descriptor. A series of ternary alloy models (such as ternary alloys with the metal elements of Ag, Pt, Ni, Fe, Au, Cu, Pd, Rh, Co, and Ru) were constructed using Jamip software. The DFT results showed that none of the single metal surfaces satisfy the description of an efficient FOR catalyst. Furthermore, analyzing the stable adsorbed G_{*CO} and G_{*OH} on various surface sites showed that the single metal may not reach the peak of the volcano plot due to its inherent characteristics. Interestingly, both ternary alloys are found to simultaneously fit the efficient adsorption of *CO and *OH for FOR catalysts, appearing closer to the volcano peak, ultimately resulting in superior FOR performance. Compared to the ternary alloys of PdPtRh, RhPdNi, PdCuAg and PdCuPt, the PdCuNi alloy is positioned at the apex of the selected volcano plot, indicating its theoretically high reactivity towards FOR.

Through the decision tree model, ternary alloy catalysts with high-performance activity can make decisions based on some of the determining conditions. At first, we established a comprehensive database by encompassing 392 sets of high-quality data for FOR catalysts (Table S2) from the previous studies. Various determining factors were taken into consideration, including the elemental composition, characteristic size, and intrinsic properties like the electrochemical surface area (ECSA) of the catalyst (Table S3). Additionally, surface microenvironmental factors like formic acid concentration, as well as experimental synthesis conditions such as annealing or dealloying treatments, were also considered. Ultimately, MA was identified as the key determining indicator for the performance of the catalyst, serving as the prediction target for the ML model.

In Fig. 1(c), feature engineering analysis was conducted on the obtained database. In the decision tree model, 90% of the data in the database was utilized as the training set to establish decision boundaries, whereas the remaining 10% served as the testing set to assess the MA of the FOR electrocatalysts. ECSA is prioritized as the root node in the analysis as a large ECSA value signifies catalysts with a substantial active area, making it a crucial factor for researchers in the design of catalyst structures. Furthermore, the decision tree identifies annealing as a significant factor that can also influence catalytic performance because the annealing process plays a crucial role in evenly distributing alloy elements, reducing material strain, and enhancing material stability. Positioned near the root node, annealing is capable of accurately classifying three data points with minimal conditions. As illustrated in Fig. S1, to clarify how various features affect the core learning objective—specifically the MA of FOR—an ensemble algorithm, RFR, was utilized. These algorithms assessed the features through the feature importance score. For RFR, the three most significant factors influencing the MA of the catalyst in the FOR remain consistent. These factors are the intrinsic ECSA of the catalyst, the characteristic size, and the concentration of formic acid. By carefully designing the top layer of the catalyst, a substantial enhancement in the performance of the FOR can be achieved. Regarding the elemental composition of the catalyst, elements such as Pd and Cu have garnered higher feature importance scores in RFR and ETR analyses, suggesting that PdCu-based alloy catalysts can achieve outstanding performance in FOR. Moreover, the supporter, annealing process, and electrolyte types garnered high rankings in the feature importance score, highlighting the profound effect of the material's synthesis

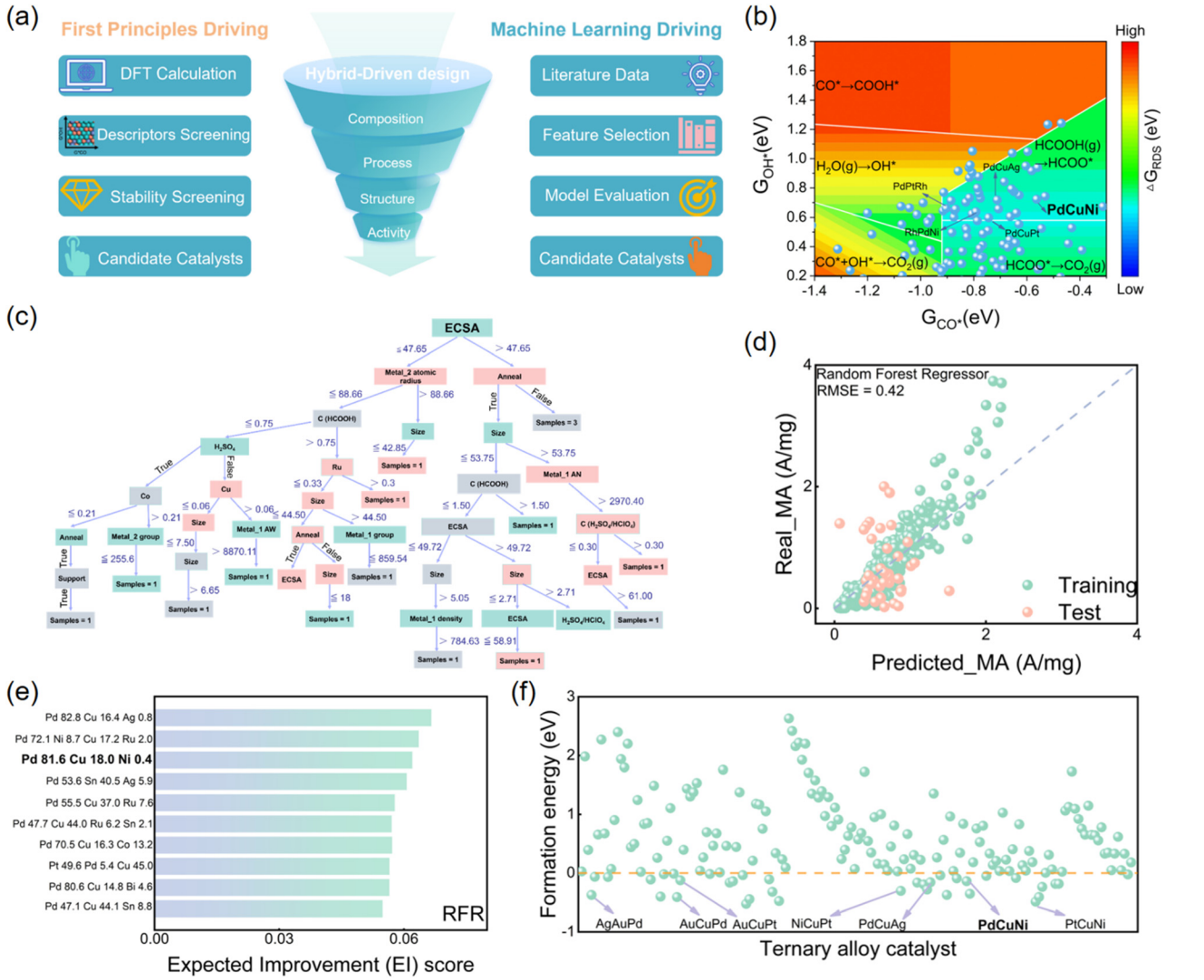

Fig. 1 Hybrid driving design of the FOR electrocatalysts. (a) Design flowchart of the FOR electrocatalyst driven by DFT calculations and ML technology. (b) High-activity FOR electrocatalyst screening combining first principles and volcano plots for ternary alloys. (c) The decision tree model for exploring the data-driven prediction of factors influencing FOR, based on a 10-fold cross validation using random forest regressor. (d) High-throughput data-driven prediction based on SMAC of random forest regressor. (e) The decision tree visualization structure used to describe the maximum mass activity of the FOR electrocatalysts. (f) Selection of the stability of ternary alloy catalysts based on the formation energy.

method on its catalytic performance. In data analysis (Fig. S2), the correlation coefficient holds paramount importance, as factors like the ECSA, Pd content, and formic acid concentration exhibit a robust positive correlation with MA. A negative correlation exists between factors like the characteristic size, Mn content, and the MA. This finding aligns well with the outcomes of the feature importance analysis and decision tree analysis. Additionally, there is a strong negative correlation between the ECSA of the catalyst and other factors, including the characteristic size, Pt content, and Ru content. In Fig. S3, Fig. 1(d) and Table S4, a total of 15 ML methods were employed to learn and predict the given MA features. The horizontal axis of the visualization represents the predicted MA through ML, while the vertical axis depicts the actual MA that was obtained by experimental testing.

To comprehensively evaluate the accuracy of the model prediction, the RMSE and the correlation coefficient R^2 were selected as metrics. Meanwhile, kernel ridge regression (KRR) and Xgboost display signs of overfitting. Compared to the prediction accuracy of various methods, the results indicate that the nonlinear tree ensemble method based on decision trees (RFR) exhibits commendable performance on both evaluation metrics, which include a RMSE of 0.42 and a correlation coefficient R^2 of 0.58 (Fig. 1(d)). The core advantages of RFR from the tree ensemble structure are that it enables excellent nonlinear modeling, handles complex feature interactions, and provides strong robustness and generalization. More importantly, DFT and ML results offer an innovative perspective for designing excellent FOR catalysts of the PdCuNi alloy with the optimal Pd/Cu/Ni atom ratio through descriptor and RFR

model engineering, resulting in a more favorable tradeoff between MA and stability.

Employing the SMAC model to approximate the genuine objective function, Expected improvement (EI) was adopted as the criterion for selection.[48] Subsequently, a high-throughput screening was conducted on 500 000 sets of unknown space alloy catalysts, leveraging the RFR method, which had demonstrated superior performance in model construction. Fig. 1(e) highlights the top 10 catalysts with the highest EI score, indicating that machine learning identifies a significant number of PdCu-based alloys as potential high-activity FOR electrocatalysts. Specifically, PdCuNi, PdCuAg, and PdCuSn catalysts demonstrate favorable performance in the RFR predictions.

In the realm of heterogeneous catalysis, achieving a delicate equilibrium between the catalyst activity and alloy stability has garnered significant research attention. In Fig. 1(f), the stability analysis of the devised ternary alloy model underscores the remarkable performance of the PdCuNi catalyst in terms of both FOR activity and thermodynamic stability. Consequently, a design of the PdCuNi catalyst driven by a hybrid approach of ML and DFT was selected for in-depth investigation.

2.2. Synthesis and structural characterization of PdCuNi AA

The PdCuNi AA catalysts were synthesized by an excessive $NaBH_4$-reduction method, and the process is illustrated by the schemes shown in Fig. 2(a) and Fig. S4. The transmission electron microscopy (TEM) image of Fig. 2(b) reveals the aerogel morphology of PdCuNi AA with a self-supporting nanostructure composed of alloy nanoparticles, possessing a high specific surface area and a significant number of mesopores (with a diameter of about 20 nm), revealing a dense network of interconnected nanowires with diameters of less than 10 nm (the inset in Fig. 2(b)). This mesoporous network structure offers abundant active sites and efficient transport channels

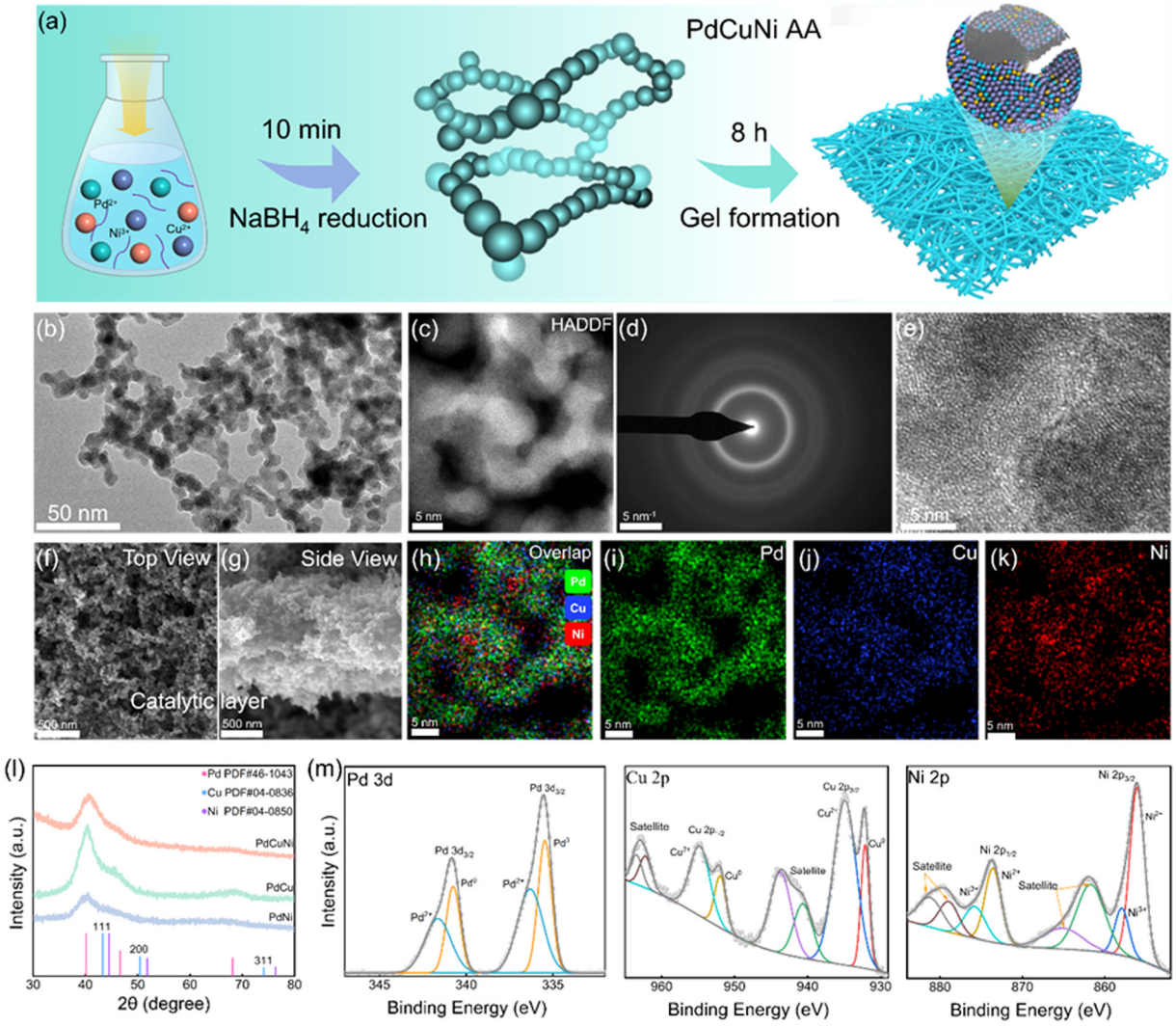

Fig. 2 Morphology and structure characterizations of PdCuNi AA. (a) Schematic of the synthesis and formation of PdCuNi AA. (b) TEM image. The inset shows diameter size distribution. (c) HAADF-STEM image. (d) SAED pattern. (e) Enlarged HRTEM image, showing a disorder arrangement lattice structure of PdCuNi AA. SEM image of the PdCuNi AA catalyst layer with the (f) top view and (g) side view. HAADF-STEM image with EDS elemental mapping of (h) overlap, (i) Pd, (j) Cu, (k) Ni. (l) XRD pattern. XPS spectra of (m) Pd 3d, (n) Cu 2p and (o) Ni 2p.

for facilitating FOR. The aberration-corrected high-angle annular dark field imaging (HAADF-STEM) (Fig. 2(c)) of PdCuNi AA and the corresponding selected area electron diffraction (SAED) pattern (Fig. 2(d)) confirm the wide halos and highly disordered arrangement of atoms without grain boundaries. This observation can be further revealed by the enlarged high-resolution transmission electron microscopy (HRTEM) (Fig. 2(e)) image with no visible crystal lattice, showing an amorphous state. The amorphous structure of the PdCuNi amorphous alloy results from both the extremely fast ion reduction kinetics during synthesis and the significant lattice differences among the Pd, Cu, and Ni constituents. These induce geometric dislocations during atomic stacking, leading to an amorphous phase rather than crystalline order. In addition, as indicated in Table S5, the atomic ratio of Pd/Cu/Ni (53.2/26.5/20.3) measured by energy dispersive spectroscopy (EDS) is close to the initial feeding ratio of 2/1/1, ensuring the synthesis of a highly disordered PdCuNi AA with a precisely controlled atomic composition. Moreover, HAADF-STEM and corresponding EDS clearly reveal the uniform distribution of Pd, Cu and Ni elements, demonstrating a homogeneous distribution of PdCuNi alloy nanoparticles over the entire aerogel (Fig. 2(c and h–k)). The electron microscopy characterization conducted using high-resolution scanning electron microscopy (SEM) reveals that the PdCuNi AA exhibits a thickness of merely 2 μm with a Pd loading of 0.07 mg cm^{-2} (Fig. 2(f–g)). Such a thin catalyst layer possesses significant advantages in terms of active site utilization and charge transfer efficiency. X-ray diffraction (XRD) analysis was employed to investigate the crystallinity and microcrystalline size of the alloy aerogels. As presented in Fig. 2(l) and Fig. S6, PdCu alloy aerogels (PdCu AAs) and PdNi alloy aerogels (PdNi AAs) were prepared as comparative samples with the same synthetic method, whose ligament sizes of 7.24 nm and 6.17 nm are similar to that of PdCuNi MEA, respectively, and the morphology structures of PdCu AAs and PdNi AAs are displayed in Fig. S7(a, b) and S8(a, b), respectively. Such a design ensures a high degree of consistency in the macroscopic structure of the samples, thereby being able to more accurately reveal the differences in the intrinsic properties of the catalysts. The XRD pattern of PdCuNi AA shows a broad diffraction peak centered around 40°, corresponding to the (111) plane of the PdCuNi alloy, revealing the formation of a highly disordered alloy structure. In addition, both PdCu AAs and PdNi AAs exhibit highly dispersed disordered atomic structural characteristics, providing an important reference benchmark for subsequent comparative analysis. Moreover, these techniques reveal that the atomic arrangement within the alloy structure exhibits an amorphous characteristic.

X-ray photoelectron spectroscopy (XPS) analysis was performed to further elucidate the chemical state of the PdCuNi AA. In Fig. 2(m) and Fig. S9, the signal peaks of the Pd, Cu and Ni metallic state can be clearly observed and present in a partially low oxidation state. For the Pd elements, distinct deconvolution peaks are observed, corresponding to the metallic Pd^0 at binding energies of approximately 340.8 eV (Pd $3d_{3/2}$) and 335.5 eV (Pd $3d_{5/2}$).[48] Additionally, peaks associated with the Pd^{2+} species are identified at 340.7 eV and 341.6 eV. For the Cu element, the deconvolution peaks corresponding to Cu^0 are observed at 952.9 eV (Cu $2p_{1/2}$) and 932.1 eV (Cu $2p_{3/2}$), while the peaks at approximately 955.1 eV (Cu $2p_{1/2}$) and 935.1 eV (Cu $2p_{3/2}$) are attributed to the Cu^{2+} species. For the Ni element, the presence of low oxidation states of Ni^{3+} and Ni^{2+} is indicated by deconvolution peaks at approximately 873.7 eV (Ni $2p_{1/2}$) and 856.2 eV (Ni $2p_{3/2}$), respectively. These findings suggest a highly uniform dispersion of Ni atoms with relatively lower atomic ratios within the alloy. Specifically, the Ni^{2+} species correspond to deconvolution peaks at 873.5 eV and 856.2 eV, while the Ni^{3+} species correspond to peaks at 875.8 eV and 858.0 eV. The XPS results reveal the formation of metallic PdCuNi and some Pd, Cu, and Ni atoms undergo oxidation, resulting in the substitution of highly mixed components. However, some of these elements in their zero-valent state remain, representing the core material that comprises the aerogel structure.

2.3. Electrocatalytic performance of FOR in PdCuNi AA

To comprehensively assess the unique characteristic of PdCuNi AA, FOR was used as a probe reaction to evaluate their performance,[49–51] and PdCu (Pd/Cu atomic ratio of 57.24/42.76), PdNi (Pd/Ni atomic ratio of 69.47/30.53), and commercial Pd/C were included as comparative samples. A detailed exploration of the FOR electrochemical performance of the four catalysts was undertaken within a three-electrode system by leveraging the hybrid drive and structural insights. As depicted in Fig. 3(a), the four catalysts exhibited stable cyclic voltammetry (CV) curves when tested in an N_2-saturated 0.5 M H_2SO_4 solution at a scanning rate of 50 mV s^{-1}. The PdCuNi alloy exhibits characteristic regions that are analogous to those of PdCu, PdNi, and Pd/C, specifically: a potential range of −0.2 V to 0 V *vs.* SCE for hydrogen adsorption and desorption, a peak adsorption range of 0.2 V to 0.4 V *vs.* SCE for Cu–O bonding, and a region spanning 0.4 V to 0.6 V *vs.* SCE encompassing both the adsorption and desorption of *OH groups, as well as the reduction of Pd–O bonds. The electrochemically active surface areas (ECSAs) of the four catalysts were determined by integrating the hydrogen adsorption/desorption peaks area or the Pd–O reduction peak in the electrochemical measurements. Given the inherent limitations in the hydrogen adsorption/desorption on the Pd surface, the peak area under the Pd–O reduction was utilized in this study to accurately quantify the ECSA.[52] The ECSA of the PdCuNi AA is 32.5 m^2 g^{-1}, significantly surpasses that of PdCu (28.9 m^2 g^{-1}), PdNi (25.3 m^2 g^{-1}), and Pd/C (21.9 m^2 g^{-1}), demonstrating that the PdCuNi AA possesses a substantial quantity of defects and surface Pd-exposed active sites, both of which are pivotal for FOR. The reduction peak of PdCuNi for the *OH intermediates falls within the range exhibited by Pd/C, PdCu, and PdNi, suggesting that it possesses a moderate adsorption energy for the *OH intermediate, which plays a pivotal role in enhancing the *CO oxidation during the FOR, and the moderate adsorption energy of *OH is crucial for facilitating the kinetic progression of this reaction. The FOR performance of PdCuNi AA was measured in 0.5 M H_2SO_4 + 0.5 M

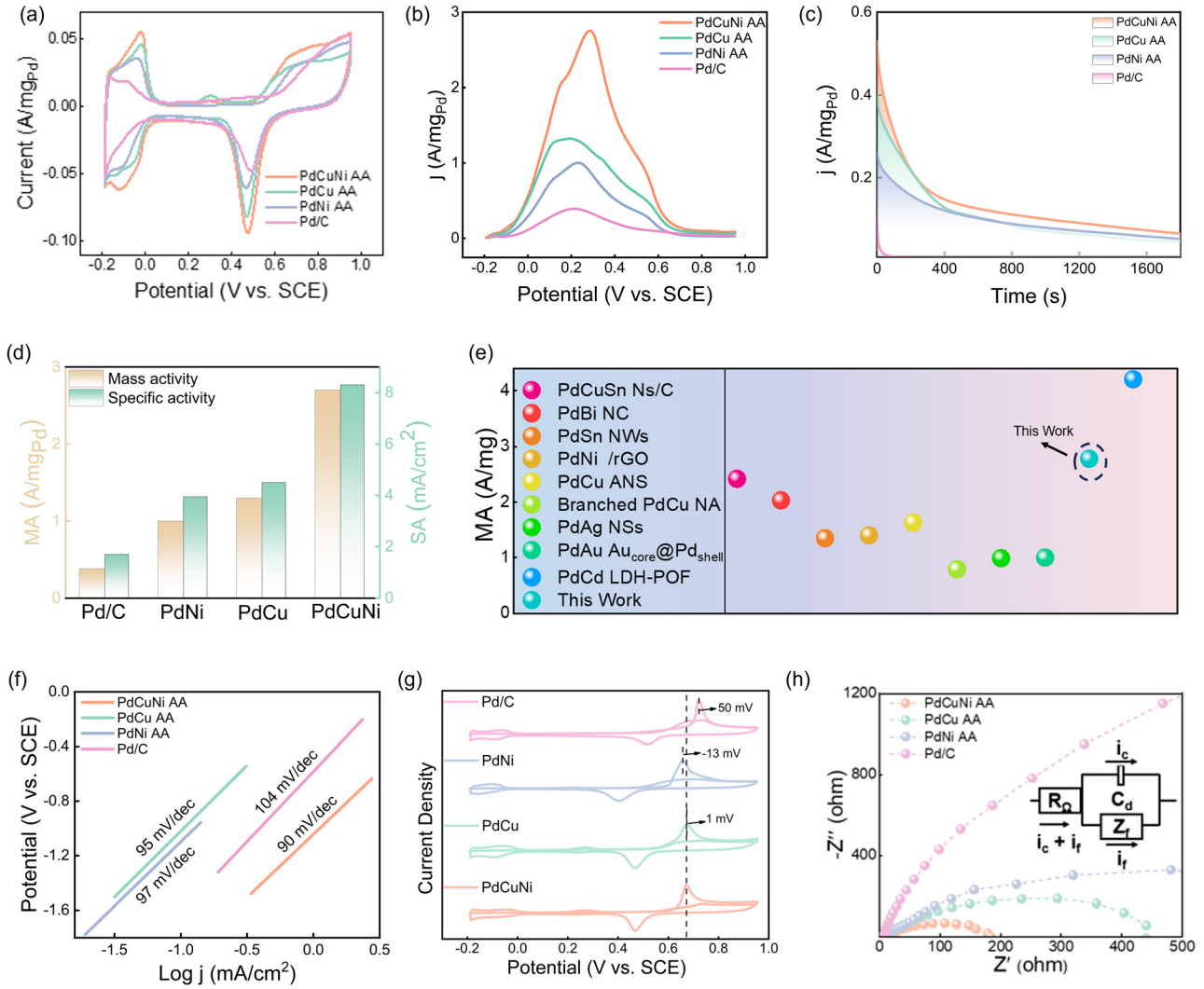

Fig. 3 FOR electrocatalytic performance evaluation of PdCuNi AA. (a) CV curves of PdCuNi AA, PdNi AAs, PdCu AAs and commercial Pd/C recorded in 0.5 M H_2SO_4. (b) Forward-scan CV curves for FOR performed in 0.5 M H_2SO_4 + 0.5 M HCOOH electrolyte with a scan rate of 50 mV s^{-1}. (c) CA curves of the four catalysts tested at 0 V *vs.* SCE. (d) Histogram of the mass activity and specific activities of commercial Pd/C, PdNi AA, PdCu AA and PdCuNi AA catalysts. (e) Mass activity comparison between PdCuNi AA and other reported catalysts for FOR. (f) Tafel plots of the four catalysts. (g) CO-stripping curves tested in N_2-saturated 0.5 M H_2SO_4 solution at a scan rate of 20 mV s^{-1} for commercial Pd/C, PdNi AA, PdCu AA and PdCuNi AA catalysts. (h) Nyquist plots of commercial Pd/C, PdNi AA, PdCu AAs and PdCuNi AA catalysts in 0.5 M HCOOH + 0.5 M H_2SO_4 with a frequency range from 0.05 to 10^5 Hz, and the inset shows the equivalent circuit.

HCOOH at a scanning rate of 50 mV s^{-1}, and compared with those of PdCu AAs, PdNi AAs and commercial Pd/C. As shown in Fig. 3(b and d), the sample was subjected to a forward scan CV test. The PdCuNi AA exhibits the highest mass activity (MA) of 2.7 A mg^{-1}, which is 2.1-, 2.7- and 6.9-folds higher than those of PdCu AAs of 1.3 A mg^{-1}, PdNi AAs of 1.0 A mg^{-1} and commercial Pd/C of 0.4 A mg^{-1}, respectively. By normalizing the peak currents with ECSAs, the PdCuNi AA displays a specific activity (SA) of 8.3 mA cm^{-2}, which surpasses those of PdCu (4.5 mA cm^{-2}), PdNi (4.0 mA cm^{-2}), and Pd/C (1.7 mA cm^{-2}) in Fig. S10. Apparently, the PdCuNi AA catalyst has the highest MA and SA for FOR among all the catalysts investigated in this study. Furthermore, the FOR performance of PdCuNi AA is even better than most of the reported catalysts (Fig. 3(e) and Table S6).

To quantitatively assess the FOR kinetics of PdCuNi AA catalysts, Tafel plots of the PdCuNi AA, PdCu AAs, PdNi AAs, and Pd/C catalysts were obtained, as illustrated in Fig. 3(f). The results show that PdCuNi AA (90 mV dec^{-1}) exhibits a smaller Tafel slope than PdCu (95 mV dec^{-1}), PdNi (97 mV dec^{-1}), and Pd/C (104 mV dec^{-1}), indicating that the PdCuNi AA surface has a more favorable FOR kinetic process. Meanwhile, electrochemical impedance spectroscopy (EIS) measurements were performed at 0.4 V to also analyze the reaction kinetics (Fig. 3(h)). These Nyquist plots were capable of being fitted using an equivalent circuit, as depicted in the inset of Fig. 3(h). In this circuit, R_Ω represents the bulk intrinsic resistance of the electrochemical system, while Z_f signifies the faradaic charge transfer resistance that arises from the FOR. Among them,

PdCuNi AA (178 Ohm) exhibits lower faradaic charge transfer resistance than PdCu AA (439 Ohm), PdNi AA (801 Ohm) and Pd/C (184 Ohm). This excellent performance is derived from the synergistic promotion effect of the PdCuNi heterostructure: the electronic structure regulation of the alloy components effectively reduces the interfacial charge transition energy barrier and accelerates the conduction of the Faraday current. At the same time, the time scale difference between the charge transfer and double-layer relaxation in PdCuNi AA is more significant. The interfacial charge is more likely to be efficiently transported through the low-energy barrier FOR. PdCuNi AA has the lowest charge transfer resistance, which confirms that its electrode interface charge transfer process is more efficient, providing kinetic support for its excellent FOR catalytic performance.

To investigate the anti-CO poisoning ability of PdCuNi AA, CO-stripping voltammograms were tested in a N_2-saturated 0.5 M H_2SO_4 solution at a scan rate of 20 mV s^{-1} (Fig. 3(g)). In comparison with Pd/C and PdCu AA, the PdCuNi AA and PdNi AA display a significantly lower potential for the CO oxidation peak. This confirms the significant contribution of more direct pathway currents that occur without the formation of *CO, along with the enhanced *CO anti-poisoning capability exhibited by PdCuNi AA. Based on the above electrochemical results, it is shown that the alloy effect has a positive promoting effect between the weak adsorption of the active site and the *CO intermediate. Through the synergistic effect of the simultaneous incorporation of Ni and Cu, the oxidation state of the Pd active site is adjusted, thereby changing its adsorption behavior to the intermediate. Consequently, the exceptional inherent stability and anti-poisoning capability of PdCuNi AA are attributable to the enhanced durability demonstrated by the FOR. The ECSA values determined by CO-stripping in an N_2-saturated 0.5 M H_2SO_4 solution at a scan rate of 20 mV s^{-1} was 38.0 m^2 g^{-1} for PdCuNi-AA, 36.1 m^2 g^{-1} for PdCu, 30.4 m^2 g^{-1} for PdNi, and 22.8 m^2 g^{-1} for Pd/C. These results confirm that the ECSA values obtained from the Pd–O reduction peak method are comparable to those measured *via* CO stripping, thus validating the reliability of the Pd–O reduction peak method.

Stability serves as a significant parameter in evaluating the practicality of a catalyst.[53,54] As depicted in Fig. 3(c), the stabilities of the PdCuNi AA, PdCu AAs, PdNi AAs and Pd/C catalysts were thoroughly tested by the chronoamperometric (CA) curves recorded in a 0.5 M H_2SO_4 + 0.5 M HCOOH solution under a constant potential of 0 V *vs.* SCE for 1800 s. The PdCuNi AA exhibits a higher initial current density than the PdCu, PdNi, and Pd/C catalysts, which indicates the high electrochemical activity of PdCuNi AA. The initial high current density stems from the complete activation of HCOOH molecules and the high concentration of unsaturated active sites. However, the rapid decline in current observed during the FOR can be ascribed to the swift reaction of *HCOOH around the catalyst, resulting in the accumulation of intermediates around the active sites and a corresponding drop in the *HCOOH concentration. After the 1800 s test, the PdCuNi AA catalyst exhibited a superior current density compared to PdCu, PdNi, and Pd/C, thereby further validating its exceptional activity and durability. After FOR, the PdCuNi AA catalyst still maintains a stable structure. As shown in Fig. S11–S13, only a small amount of the XRD (111) peak position shifted to the left due to lattice expansion and the slightly coarsened average ligament size of 8.36 nm (inset of Fig. S11). As shown in Fig. S12, the EDS energy spectrum results show that the Ni atomic ratio after the cycle is 0.27%, indicating that the preferential oxidation of Ni in the electrochemical test is one of the main reasons for the deactivation of the catalyst. In PdCuNi AA, Cu and Ni can act as ''sacrificial sites'' to preferentially participate in the oxidation reaction and protect the active center of Pd. In summary, the PdCuNi AA have been successfully designed *via* hybrid driving methodology, demonstrating the outstanding FOR activity and stability.

2.4. DFFCs and assisted hydrogen production performance application

Given the exceptional activity and stability of the PdCuNi AA towards FOR, we conducted a comprehensive evaluation of the practical application in the DFFCs system. Compared to the conventional catalyst layers loaded on carbon supports, the unsupported thin catalyst layer (UTCL) exhibits marked improvements in activity, stability, and cost-effectiveness. Its self-supporting structure eliminates the risk of noble metal particle agglomeration and detachment associated with carbon support corrosion.[55] The single-cell membrane electrode assembly (MEA) constructed by self-supporting PdCuNi AA anode UTCL was assembled for the controlled polarization curves and constant voltage durability measurements (Fig. S14). The single cell structure of DFFCs and the DFFCs test system are shown in Fig. 4(a) and Fig. S15, respectively. The UTCL has good compatibility with the proton exchange membrane. Due to its excellent mechanical stiffness and continuous structural characteristics, it has better properties than the supported catalyst layer in the heat transfer, mass transfer and highly proton conductive processes in anode UTCL. Using advanced self-assembly technology on the surface of the gas diffusion layer, we successfully designed and constructed an ultra-thin, porous, and three-dimensional UTCL, which exhibited an excellent power density performance. In DFFCs, the anode catalyst layer thickness has a highly sensitive and non-monotonic impact on the FOR performance. Performance can be severely restricted when the catalyst layer is too thin or too thick. An overly thin layer provides limited catalyst surface area, resulting in scarce active sites and a significant reduction in the FAO reaction rate. Conversely, a thick layer structure hinders the diffusion of liquid formic acid to internal active sites. Simultaneously, the product CO_2 accumulates in the deep regions of the pores, resulting in gas clogging that severely hampers mass transport. Fig. 4(b) displays the steady-state polarization curves of the PdCuNi AA UTCLs with different loadings of 0.35 mg cm^{-2}, 0.5 mg cm^{-2} and 1.5 mg cm^{-2} and the PdCuNi AA UTCL without carbon support. A maximum power density of 202 mW cm^{-2} was obtained with 0.5 mg cm^{-2},

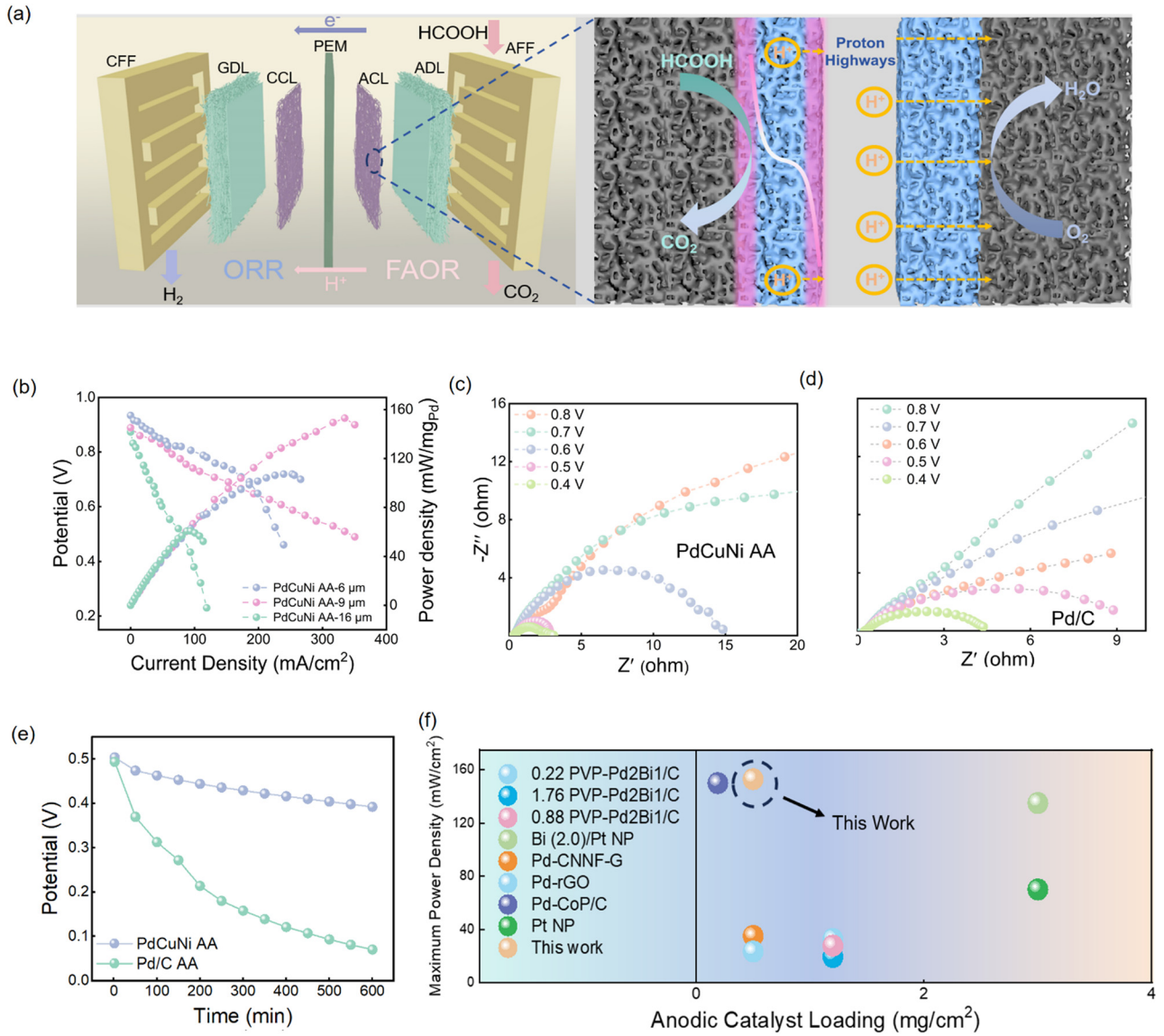

Fig. 4 (a) Schematic of the DFFCs single cell with anode PdCuNi AA UTCL. (b) Steady-state polarization curves for DFFCs single cells employing PdCuNi AA UTCL as the anode at 65 °C in different loadings of 0.35 mg cm^{-2}, 0.5 mg cm^{-2} and 1.5 mg cm^{-2}. (c) and (d) Nyquist plots of PdCuNi AA and Pd/C in DFFCs. (e) Stability measurements at a current density of 50 mA cm^{-2} for a duration of 10 hours and tested at a temperature of 65 °C. (f) MEA performance of PdCuNi AA comparisons with the reported anode catalysts below 65 °C.

which is 3.5 times higher than that of commercial Pd/C (43.8 mW cm^{-2}) with the loading of 2 mg cm^{-2} (Fig. S16). This is also highly competitive among the reported Pd-based anode catalysts in DFFCS (Fig. 4(f) and Table S7). The UTCL thickness of 0.07 mg cm^{-2} is about 2 μm, and the outer surface shows a uniform morphology, thus forming a continuous and uniform MEA structure.[48]

The catalyst loading plays a core role, as it directly determines the thickness of the CL, and thus impacts the DFFCs performance. As shown in Fig. 4(b), we systematically studied the single cell performance of DFFCs at three different loadings of 0.35 mg cm^{-2}, 0.50 mg cm^{-2} and 1.5 mg cm^{-2} for the anode PdCuNi AA catalyst. Specifically, when the catalyst loading is 0.5 mg cm^{-2}, the DFFCs single cell exhibits an excellent peak current density, up to 153 mW cm^{-2}, which is significantly higher than the performance under other loading of 0.35 mg cm^{-2} (107.2 mW cm^{-2}) and dropped sharply to 60.8 mW cm^{-2} at 1.5 mg cm^{-2} loading. This phenomenon strongly proves that there is a close correlation between the UTCL loading and the DFFCs performance, and this correlation is not a simple linear relationship but is the result of the complex influence of the proton transport capacity in the UTCL as the thickness changes. It is worth noting that the PdCuNi AA catalyst achieved a peak power density of 153 mW cm^{-2} at a loading of 0.5 mg, which is a significant improvement compared to other loading conditions (compared to the lowest value increased by approximately 2.5 times), further highlighting the importance of finding the optimal UTCL thickness for

optimizing the DFFCs performance. Based on the *V–I* polarization curves tested at 65 °C, the open circuit voltage of PdCuNi AA was 0.89 V (0.5 mg cm^{-2}), which is much higher than that of commercial Pd/C (0.85 V). By comparing the faradaic charge transfer resistance of PdCuNi AA and commercial Pd/C in DFFCs (Fig. 4(c and d)) under different potential conditions, it is found that the reduction of the potential has a certain promoting effect on electron transfer. PdCuNi AA has a lower faradaic charge transfer resistance than commercial Pd/C, which means that the electron transfer resistance of PdCuNi AA is smaller than that of Pd/C in DFFCs. In addition, PdCuNi AA exhibited good stability under a constant current of 50 mW cm^{-2} for 10 h, with the voltage decaying by only 22.2%. Meanwhile, the commercial Pd/C decayed by nearly 86.0% under the same test conditions (Fig. 4(e)).

It is known that H_2 exhibits significantly higher energy density compared to conventional fossil fuels. Electrochemical water splitting technology is a promising method for producing high-purity hydrogen. The core of this process lies in two key half-cell reactions: the oxygen evolution reaction (OER) occurring at the anode and the hydrogen evolution reaction (HER) occurring at the cathode, as shown in Fig. S17(a). However, due to the sluggish kinetics of the OER reaction, a higher electrolysis potential (1.23 V) needs to be applied when performing water electrolysis under standard conditions, resulting in a significant increase in energy consumption. By selecting appropriate small-molecule substrates (such as formic acid, hydrazine hydrate, *etc.*) and substituting the sluggish anodic oxygen evolution reaction (OER) with more thermodynamically favorable oxidation reactions, efficient hydrogen production with reduced energy consumption can be achieved. HER coupling with small molecule compounds is a solution with great application prospects for hydrogen production by electrooxidation. Liu *et al.*[56] coupled HER and the ethylene glycol oxidation reaction (EGOR) to drive a current of 10 mA cm^{-2} with an applied voltage of only 1.25 V. Zhu *et al.*[57] reported a UOR electrode of Co-doped $NiMoO_4$ that lasted for 200 h without degradation at a high current of 100 mA cm^{-2}. In view of this, FOR electrocatalysts with high performance have significantly reduced the anodic electrolysis potential, indicating the broad development prospects and potential excellent applications in replacing traditional OER. While reducing the potential required in the electrolysis process, it significantly improves the hydrogen production efficiency of MEA.

As clearly shown in Fig. S17(a and b), hydrogen production using the FOR significantly reduces energy consumption. Thanks to the efficient generation of H^+ products and the excellent selective transmission capability of protons by the proton exchange membrane, this device can greatly promote the generation rate of hydrogen in the cathode region, thereby significantly enhancing its overall effectiveness and efficiency as an auxiliary means of hydrogen production.[58,59] The results are shown in Fig. S17(c). PdCuNi AA achieved a current density of 189 mA cm^{-2} at a low potential of 0.39 V, which has significant advantages over Pd/C in the ability of hydrogen production. In addition, the slight decrease in current density at high potential is attributed to the generation of side reactions in the FOR process of the anode PdCuNi AA catalyst.

2.5. Analysis of the FOR mechanism on the PdCuNi AA surface

DFT calculations were conducted to elucidate the underlying mechanism responsible for the high activity of FOR on the PdCuNi surface. Specifically, PdCuNi, PdCu, and Pd catalyst models were constructed, with PdCuNi serving as the research focus of the study, while PdCu and Pd acted as the comparative models. Electron localization function (ELF) simulation analysis was performed on the surfaces of PdCuNi, PdCu, and Pd. The results demonstrated that the electron localization near Pd atoms is slightly elevated compared to that around Ni and Cu atoms, as shown in Fig. S18. Notably, electrons in the vicinity of Ni and Cu exhibit partial accumulation around Pd atoms. This phenomenon suggests that the presence of electron-rich Pd active centers could potentially account for the high activity for FOR observed in PdCuNi.

The free energy profiles for the potential FOR on PdCuNi, PdCu, PdNi and Pd surface are displayed in Fig. 5(a). Table S8 summarises the reaction energies for FOR elementary steps over the four catalysts surfaces. This analysis resulted in the derivation of FOR Gibbs free energy step profiles for PdCuNi, PdCu, and Pd by using first-principles calculations, all referenced against the standard hydrogen electrode reaction. The adsorption of HCOOH on the catalysts was identified as the potential-determining step (PDS) and the reaction pathway of FOR on the Pd, PdCu, and PdCuNi surfaces generally followed the direct pathway *via* the two-step dehydrogenation of formic acid. The formation of *HCOO is an energy-consuming faradaic step, which inevitably becomes a key step affecting the reaction rate during the reaction process. In Fig. 5(a), the PDS of the two dehydrogenation reactions of HCOOH on the Pd(111) surface as FOR are both around 0.33 eV, essentially following the direct pathway of formic acid dehydrogenation (HCOOH(g)–*HCOO/*COOH–CO_2(g)). The PdNi, PdCu and PdCuNi surfaces both adhere to the direct pathway *via* the two-step dehydrogenation of HCOOH–CO_2(g) for formic acid, commencing from HCOOH(g) to *HCOO and ultimately to CO_2(g). Notably, PdCuNi demonstrates a lower reaction barrier of 0.18 eV, compared to PdNi (0.24 eV), PdCu (0.21 eV) and Pd (0.33 eV). This lower energy barrier signifies that the FOR proceeds at a faster rate on PdCuNi. The ML and volcano plot predictions suggest that the energy barrier for the direct oxidation of *COOH to CO_2(g) in the ternary PdCuNi alloy is lower than that for its oxidation to *CO, and lower compared to PdNi, PdCu and Pd, indicating that PdCuNi exhibits superior anti-CO poisoning activity. In summary, the PdCuNi alloy stands out among other catalysts with its reduced PDS from its distinctive electronic properties. This revelation underscores the exceptional performance, while also validating the dependability and efficacy of high-throughput ML and first-principles calculations in identifying promising catalysts.

AIMD offers an efficient approach to simulate the stability of catalysts over extended time scales. As demonstrated in Fig. S9(a and b), the stability of PdCuNi was investigated using

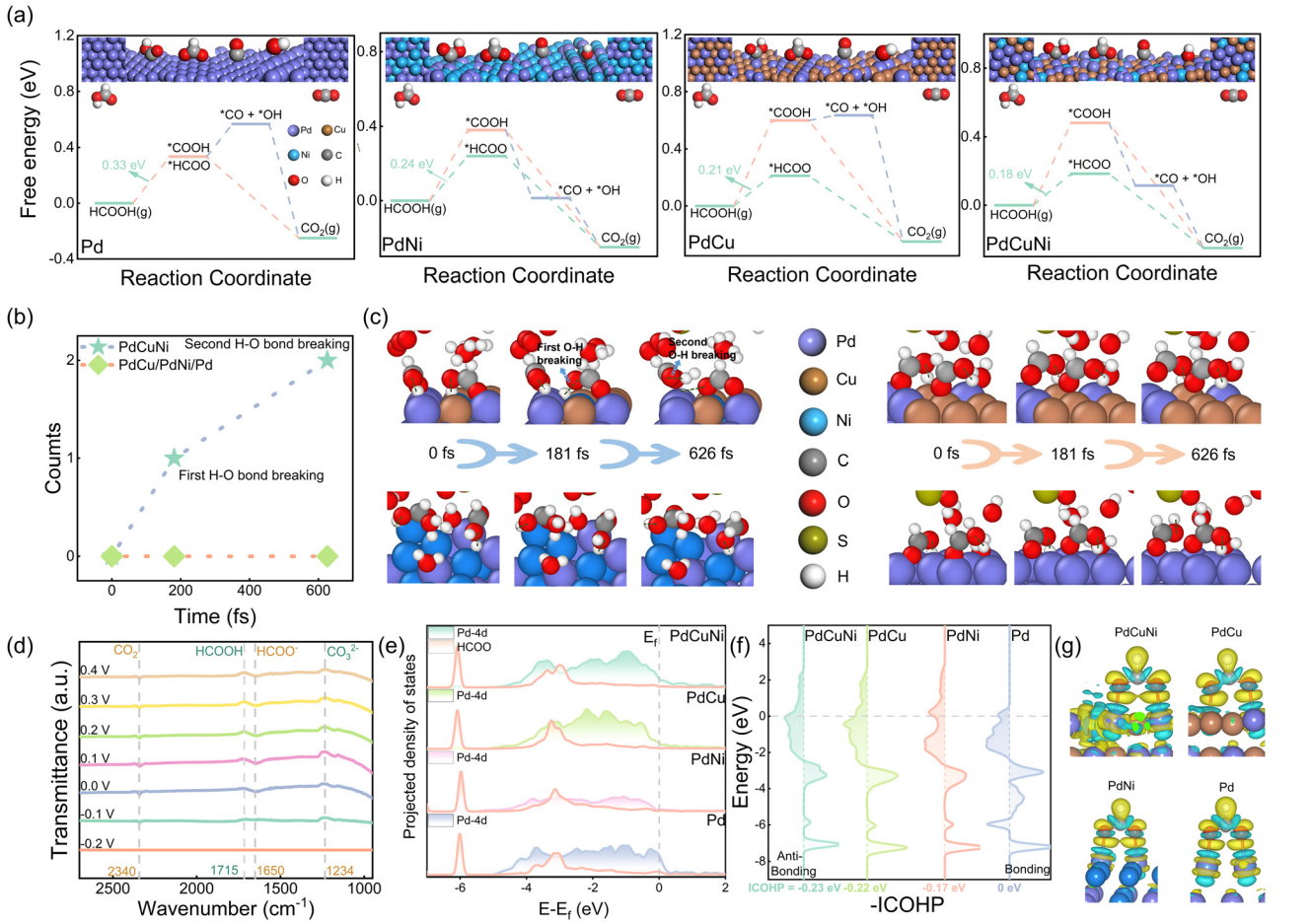

Fig. 5 (a) Free energy profiles of HCOOH adsorption and oxidation reaction over the Pd(111), PdNi(111), PdCu(111) and PdCuNi(111) surfaces. AIMD for FOR analysis: (b) simulation time and H–O bond breaking count for Pd, PdNi, PCu, PdCuNi, and the (c) FOR process over Pd, PdNi, PCu, and PdCuNi surface. (d) *In situ* FTIR spectra under the FOR process over PdCuNi AA from −0.2 V to 0.4 V (*vs.* SCE). (e) PDOS for the interaction between the PdCuNi, PdCu, and Pd surface active sites and HCOO. (f) COHP for the interaction between the PdCuNi, PdCu, and Pd surface active sites and HCOO. (g) ED (isosurface = 0.002 e Bohr^{-3}) of Pd, PdNi, PCu, PdCuNi.

AIMD under the NVT ensemble at a constant temperature of 300 K. Throughout the simulation period spanning up to 7000 fs, the PdCuNi surface structure remained notably unaltered, while the temperature and energy of the catalytic system exhibited consistent stability. The overall diffusion coefficient and RMSD of PdCuNi exhibit stability over time, reaffirming the remarkable stability of the PdCuNi catalyst. As shown in Fig. 5(b and c), to delve into the potential advantages of PdCuNi for the FOR, AIMD simulations were conducted to model the FOR process on PdCuNi PdCu PdNi and Pd surfaces in acidic solvent environment. The findings from AIMD simulations and free energy step diagrams align closely in showing that FOR proceeds *via* a direct two-step dehydrogenation pathway for PdCuNi, where *HCOOH undergoes selective dehydrogenation to form *HCOO, thereby effectively circumventing the risk of CO poisoning. Concurrently, during the initial 626 fs, the Pd/PdNi/PdCu catalyst surface failed to initiate the *HCOOH dehydrogenation reaction, whereas the PdCuNi catalyst swiftly converted HCOOH to *HCOO within that same timeframe. This observation underscores the superior FOR reaction kinetics exhibited by PdCuNi compared to the Pd, PdNi and PdCu.

To further explore the potential reaction pathway of PdCuNi AA during the FOR process, an *in situ* Fourier transform infrared (FTIR) study was carried out. FTIR possesses the distinctive capability of uncovering the evolution of various adsorbed species and products throughout the course of electrocatalytic reactions. Fig. 5(d) displays the acquired *in situ* FTIR spectra under the FOR process for PdCuNi AA from −0.2 V to 0.4 V *vs.* SCE during successive potential steps. The IR band with positive intensity at 1715 cm^{-1} signifies the progressive consumption of the reactant HCOOH during the FOR process as the potential increases. The asymmetric stretching vibration of the O═C═O group in CO_2 yields a distinctive high-intensity peak at the band around 2340 cm^{-1}, whereas the characteristic C═O stretching vibration peak of CO, typically situated around the 2100 cm^{-1} band, was notably absent. Driven fully by the electrode potential, the further oxidation of formic acid results in CO_2 becoming the anticipated product of the PdCuNi AA. CO_2 production commences at a low potential of −0.1 V *vs.* SCE.

The diminishing peak within the band at 1650 cm^{-1} signifies the *HCOO species (C–H asymmetric stretching vibration), which progressively forms as the potential increases, while no CO is produced. In summary, the intermediate and product information provided by the *in situ* FTIR spectra was consistent with the DFT result. Thus, it can be inferred that the final product CO_2 is produced by a direct pathway *via* the two-step dehydrogenation of formic acid (HCOOH (g) – *HCOO – CO_2(g)), and without the *CO intermediate produced during FOR, which reflects the strong anti-CO poisoning over PdCuNi AA.

The anti-CO poisoning ability of a catalyst is a key factor affecting its performance. Understanding its internal mechanism is conducive to designing catalysts with high activity and stability. The properties of the catalyst are determined by its electronic structure. Based on PDOS and ED, the electronic properties of CO adsorbed on the surfaces of PdCuNi, PdCu, PdNi and Pd were further analyzed to explore the potential mechanism of strong anti-CO poisoning. In Fig. S20(a–d), the degree of overlap between the PDOS of the CO intermediate and the surface of the PdCuNi, PdCu and PdNi catalysts is low, and a large amount of charge is not accumulated at the reaction interface. The Pd-4d and CO molecular orbitals only partially overlap at the low energy level, indicating that both PdCuNi, PdCu and PdNi have good anti-CO poisoning. The adsorption behaviors of PdCuNi, PdCu and PdNi exhibit striking similarities. However, a comparative analysis reveals that PdCuNi exhibits a reduced low-level antibonding orbital splitting, coupled with a more pronounced overlap between the Pd-4d and *π orbitals of CO. This underscores the effectiveness of the alloy strategy, where the incorporation of Cu and Ni optimizes the electronic structure of Pd-based alloys, significantly lowering the CO desorption energy barrier. Consequently, the PdCuNi catalyst exhibits exceptional anti-CO poisoning ability. The ED analysis presented in Fig. S20(e–h) highlights the chemical adsorption phenomenon between *CO and the catalyst surfaces. Employing Bader charge calculations, we determined the charge transfer upon CO adsorption on the three surfaces. Notably, the charge transfer for PdCuNi (0.04 e) was lower than that for Pd (0.05 e) PdNi (0.11 e) and PdCu (0.10 e). This reduced charge transfer suggests that the PdCuNi catalyst exhibits weaker CO adsorption, thereby exhibiting superior anti-CO poisoning ability. Through rigorous and in-depth research, the electronic structure analysis has unveiled the fundamental mechanism underlying exceptional thermodynamic and kinetic reaction tendencies for PdCuNi. In Fig. 5(e), the adsorption behavior of *HCOO on PdCuNi, PdCu, PdNi and Pd surfaces was investigated using PDOS analysis. The findings indicate a remarkable alignment of energy levels between *HCOO and the active sites on these surfaces, particularly in the low-energy orbitals proximate to −3.0 eV, where a pronounced coupling effect is observed. Further analysis revealed that the electron distribution of PdCuNi exhibits a distinct bias towards the Fermi level energy compared to other catalysts. This characteristic suggests that PdCuNi possesses a reduced presence of antibonding components below the Fermi level energy, leading to an enhanced interaction with *HCOO and offering robust reinforcement for its outstanding reaction performance. After a thorough analysis of the electronic structure of PdCuNi, it was observed that its electron distribution exhibits a notably higher degree of delocalization compared to PdCu, PdNi and Pd. The coupling effect with the *HCOO molecular orbital is particularly pronounced, which directly signifies a stronger interaction between PdCuNi and the *HCOO intermediates. Consequently, on the PdCuNi surface, the energy barrier associated with the faradaic reaction step of HCOOH to *HCOO, as the PDS, is significantly diminished, which effectively accelerates the FOR-reaction rate, rendering it faster on the PdCuNi surface.

As depicted in Fig. 5(f), the results of the crystal orbital Hamilton population (COHP) analysis highlight the significant advantage of PdCuNi in terms of the bonding components. This directly underscores the exceptional adsorption capacity of *HCOO over the PdCuNi surface. Specifically, the integrated crystal orbital Hamilton population (ICOHP) serves as a crucial metric, accurately gauging the intensity of the interaction between the catalyst surface and *HCOO intermediate. The analysis reveals that the ICOHP value for PdCuNi is −0.23 eV, slightly surpassing the values for PdCu (−0.22 eV), PdNi (−0.18 eV) and significantly surpassing the pure Pd (0 eV). This dataset not only validates the robust stability of the adsorption bond between PdCuNi and *HCOO, but also underscores the pivotal role of this stability in effectively lowering the energy barrier of the PDS. The results of the ED analysis presented in Fig. 5(g) demonstrate significant charge transfer occurring between *HCOO and the surfaces of PdCuNi, PdCu, PdNi and Pd, respectively. Notably, for the PdCuNi catalyst, the presence of Ni atoms on the electron-deficient surface leads to the most prominent charge transfer with *HCOO, surpassing that observed over PdCu, PdNi and Pd. This phenomenon further affirms the low energy barrier of the PDS, and the high reaction rate achieved through the stable adsorption between *HCOO and the catalyst. In essence, the robust orbital coupling between the PdCuNi catalyst and the *HCOO intermediate significantly facilitates the stable adsorption of *HCOO on the catalyst surface, thereby drastically accelerating the FOR progress on the PdCuNi surface.

In addition, the influence of Ni oxidation on the catalytic activity during the FOR process is considered. A model was constructed in which Ni atoms are covered by oxygen atoms (named PdCuNi–O) through DFT. Its electronic structure and the ability of adjacent Pd active sites to resist CO poisoning were analyzed. The local environment of mild Ni oxidation was qualitatively simulated. As shown in the figure below, the results show the following: the O coverage around Ni significantly changes the electronic structure of neighboring atoms due to its strong electronegativity, resulting in the loss of electrons by Pd atoms as the main active sites. Its d-band center (−1.59 eV) is far away from the Fermi level compared with the unoxidized PdCuNi (−1.38 eV), indicating that the adsorption of reaction intermediates by the catalyst tends to weaken after mild Ni oxidation, as shown in Fig. S20(a). The adsorption energy of CO was further compared to the two

models. The CO adsorption energy of PdCuNi–O (−1.24 eV) is lower than that of PdCuNi (−1.28 eV), which clearly proves that the slightly oxidized state of the Ni atom surface helps to improve the CO poisoning resistance of the PdCuNi AA catalyst. This represents a promoting effect on FOR, as shown in Fig. S21(b and c). For this reason, the PdCuNi AA catalytic material exhibits good stability and activity in FOR and DFFCs tests. At the same time, based on the DFT evaluation of Ni dissolution and oxidation tendency, the formation energy of Ni vacancies on the surface of PdCuNi was calculated (−0.06 eV). This value is close to neutral, indicating that the surface Ni atoms are not prone to dissolution or oxidation migration, as shown in Table S9. The discussion focuses on the specific electronic structure effects in the slightly oxidized state and their impact on specific performance (CO poisoning resistance). It should be emphasized that, based on our full understanding, excessive oxidation of the catalyst (such as the formation of a large amount of Ni oxide on the surface) will cover the active sites, which is obviously not conducive to the catalytic reaction.

3. Conclusions

In this work, a hybrid ML and first-principles approach was used to extract 392 sets of data from the literature to build an ML database and the RFR model was used to search for 500 000 catalysts in the unknown space. Combined with high-throughput first-principles results, PdCuNi alloy catalysts with high activity and stability were screened. PdCuNi AA catalysts with disordered atomic arrangement were successfully designed and synthesized for FOR. The catalyst possesses a noteworthy MA of 2.7 A mg^{-1}, significantly surpassing commercial Pd/C by a factor of approximately 6- to 9-folds. Furthermore, it achieves an impressive power density of up to 153 mW cm^{-2} in DFFCs. Additionally, the water electrolysis cell tests exhibited an impressive current density of 189 mA cm^{-2}, achieving a low potential of 0.39 V. The synergistic combination of advanced techniques such as first principles and ML holds immense potential in pioneering innovative catalyst design, thereby playing a pivotal role in propelling the development of new energy fields.

Author contributions

Pengcheng Liu: methodology, formal analysis, writing – original draft. Dezhi Su: conceptualization, data curation. Xiao Chen: data curation. Yanyi Liu: investigation, validation. Kaili Wang: supervision, writing – review & editing. Da Chen: supervision, resources. Xijun Liu: supervision, resources. Jia He: conceptualization, project administration, funding acquisition.

Conflicts of interest

There are no conflicts to declare.

Data availability

The authors will supply the relevant data in response to reasonable requests.

Supplementary information is available. See DOI: **https://doi.org/10.1039/d5ey00149h**

Acknowledgements

This work was financially supported by the National Natural Science Foundation of China (52073214). This work was also supported by the open research fund of the Laboratory of Xinjiang Native Medicinal and Edible Plant Resources Chemistry at Kashi University. We gratefully acknowledge HZWTECH for providing computation facilities. This research was supported by the Tian-He Qingsuo open research fund of TSYS in 2022 & NSCC-TJ. We also thank Nankai University Large-scale Instrument Experimental Technology R&D Project No. 21NKSYJS09.

Notes and references

1 S. Huang, J. Li, X. S. Wang, Y. S. Kang, Y. J. Zhao, H. Wang, P. X. Zhang, L. Zhang and C. Y. Zhao, *ACS Appl. Mater. Interfaces*, 2023, **15**, 14447–14456.
2 X. R. Hu, W. Z. An, W. Z. Wang, X. Lin, T. S. Chan, C. H. Zhan, Z. W. Hu, X. Q. Yang and L. Z. Bu, *J. Am. Chem. Soc.*, 2023, **145**, 19274–19282.
3 G. A. El-Nagar, K. M. Dawood, M. S. El-Deab and B. E. Al-Andouli, *Appl. Catal., B*, 2017, **213**, 118–126.
4 K. L. Wang, D. Y. Huang, Y. C. Guan, F. Liu, J. He and Y. Ding, *ACS Catal.*, 2021, **11**, 14428–14438.
5 Q. Sang, S. Yin, F. Liu, H. Yin, J. He and Y. Ding, *Nano Res.*, 2021, **14**, 3502–3508.
6 C. Y. Dong, B. Zhang, H. J. Song, S. Y. Zhou, J. Y. Ye, H. G. Liao, L. S. Dong and L. Z. Bu, *ACS Nano*, 2024, **18**, 10008–10018.
7 X. M. Ning, L. Zhan, X. S. Zhou, J. Luo and Y. L. Wang, *J. Colloid Interface Sci.*, 2024, **655**, 920–930.
8 C. Y. Dong, X. Y. Wang, Z. P. Zhu, C. H. Zhan, X. Lin, L. Z. Bu, J. Y. Ye, Y. C. Wang, W. Liu and X. Q. Huang, *J. Am. Chem. Soc.*, 2023, **145**, 15393–15404.
9 X. B. Fu, H. J. Li, A. N. Xu, F. J. Xia, L. Zhang, J. H. Zhang, D. S. Ma, J. S. Wu, Q. Yue, X. Yang and Y. J. Kang, *Nano Lett.*, 2023, **23**, 5467–5474.
10 Q. Zhang, Y. H. Xie, X. Zhang, M. X. Zhao, Q. Chen, Y. M. Wu, J. F. Yu, Q. Y. Pan, F. Q. Yang and H. H. Lin, *ChemCatChem*, 2023, **15**, e202300255.
11 X. Zhang, H. T. Chen, K. P. Li, B. Wen, J. Ma and Q. Wu, *ACS Appl. Nano Mater.*, 2024, **7**, 14288–14296.
12 S. Y. Jin, Y. H. Li, Y. P. Yang and W. Zhang, *Mater. Today Nano*, 2024, **26**, 100485.
13 J. S. Tian, Y. C. Hu, W. F. Lu, J. H. Zhu, X. D. Liu, J. Shen, G. Wang and J. Schroers, *Carbon Energy*, 2023, **5**, e322.

14 Y. Z. Li, J. L. Tang, H. L. Zhang, Y. Y. Wang, B. Lin, J. C. Qiao, H. P. Zheng, Z. X. Yu, Z. X. Liu, Y. D. Liu, T. G. Zhou and X. Z. Lei, *Chem. Eng. J.*, 2023, **453**, 139905.
15 W. C. Wang, T. N. He, X. L. Yang, Y. M. Liu, C. Q. Wang, J. Li, A. D. Xiao, K. Zhang, X. T. Shi and M. S. Jin, *Nano Lett.*, 2021, **21**, 3458–3464.
16 C. Q. Pei, S. Q. Chen, T. C. Zhao, M. Li, Z. T. Cui, B. A. Sun, S. G. Hu, S. Lan, H. Hahn and T. Feng, *Adv. Mater.*, 2022, **34**, 2200850.
17 J. Johny, M. Kamp, O. Prymak, S. X. Liang, T. Krekeler, M. Ritter, L. Kienle, C. Rehbock, S. Barcikowski and S. Reichenberger, *Nano Res.*, 2022, **15**, 4807–4819.
18 Y. G. Zhao, J. J. Liu, C. G. Liu, F. Wang and Y. Song, *ACS Catal.*, 2016, **6**, 4127–4134.
19 P. Yang, Y. P. An, C. R. Feng, Y. X. Liu, B. Liu, L. Q. Gao, Y. Q. Zhou, X. M. Li, P. Li and F. G. Zeng, *Int. J. Hydrogen Energy*, 2024, **51**, 1218–1228.
20 A. A. Peterson and J. K. Nørskov, *J. Phys. Chem. Lett.*, 2012, **3**, 251–258.
21 R. Ignatans, G. Mallia, E. Ahmad, L. Spillane, K. A. Stoerzinger, S. H. Yang, N. M. Harrison and V. Tileli, *J. Phys. Chem. C*, 2019, **123**, 11621–11627.
22 W. Q. Feng, H. Chen, Q. Zhang, R. Q. Gao and X. X. Zou, *Chin. J. Catal.*, 2020, **41**, 1692–1697.
23 J. Wang, Y. Y. Song, C. Chen, X. Zhao and W. L. Fan, *ACS Catal.*, 2023, **13**, 15794–15810.
24 X. B. Liao, R. H. Lu, L. X. Xia, Q. Liu, H. Wang, K. Zhao, Z. Y. Wang and Y. Zhao, *Energy Environ. Mater.*, 2022, **5**, 157–185.
25 A. Vojvodic and J. K. Nørskov, *Science*, 2011, **334**, 1355–1356.
26 G. A. Tritsaris and J. Rossmeisl, *J. Phys. Chem. C*, 2012, **116**, 11980–11986.
27 J. K. Nørskov, T. Bligaard, J. Rossmeisl and C. H. Christensen, *Nat. Chem.*, 2009, **1**, 37–46.
28 C. J. Chen, H. Y. Jin, P. T. Wang, X. G. Sun, M. Jaroniec, Y. Zheng and S. Z. Qiao, *Chem. Soc. Rev.*, 2024, **53**, 2022–2055.
29 J. T. Bender, A. S. Petersen, F. C. Østergaard, M. A. Wood, S. M. Heffernan, D. J. Milliron, J. Rossmeisl and J. Resasco, *ACS Energy Lett.*, 2023, **8**, 657–665.
30 X. Liu and M. T. Koper, *J. Am. Chem. Soc.*, 2024, **146**, 5242–5251.
31 T. Liu, Y. Wang and Y. Li, *JACS Au*, 2023, **3**, 943–952.
32 X. L. Yang, Q. L. Meng, X. Wang, Z. Jin, C. P. Liu, J. J. Ge and W. Xing, *J. Energy Chem.*, 2022, **71**, 188–191.
33 L. C. Liang, M. Li, B. T. Zhang, J. H. Liang, B. W. Zeng, L. M. Wang, Y. W. Tang, G. T. Fu and Z. M. Cui, *Adv. Energy Mater.*, 2023, **13**, 2203803.
34 C. Chen, Y. X. Zuo, W. K. Ye, X. G. Li, Z. Deng and S. P. Ong, *Adv. Energy Mater.*, 2020, **10**, 1903242.
35 O. Isayev, D. Fourches, E. N. Muratov, C. Oses, K. Rasch, A. Tropsha and S. Curtarolo, *Chem. Mater.*, 2015, **27**, 735–743.
36 R. Ding, Y. Q. Ding, W. J. Yin, Y. D. Liu, J. Li and J. G. Liu, *Angew. Chem., Int. Ed.*, 2020, **59**, 19175–19183.
37 S. Griesemer, Y. Xia and C. Wolverton, *Nat. Comput. Sci.*, 2023, **3**, 934–945.
38 P. Liu, Y. Liu, K. Wang, S. Shi, M. Jin, J. Liu, T. Qin, Q. Liu, X. J. Liu and J. He, *Nano Res.*, 2024, **17**, 7957–7966.
39 W. Wang, W. L. Jing, F. X. Wang, S. J. Liu, X. Y. Liu and Z. Q. Lei, *J. Power Sources*, 2018, **399**, 357–363.
40 D. D. Zhang, H. B. Li, H. J. Lu, Z. Y. Yin, Z. Fusco, A. Riaz, K. Reuter, K. Catchpole and S. Karuturi, *Energy Environ. Sci.*, 2023, **16**, 5065–5075.
41 Y. Nakaya and S. Furukawa, *Chem. Rev.*, 2023, **123**, 5859–5947.
42 Z. S. Li, B. L. Li, M. Yu, C. L. Yu and P. K. Shen, *Int. J. Hydrogen Energy*, 2022, **47**, 26956–26977.
43 J. Y. Ding, H. Yang, H. Zhang, Z. F. Wang, Q. Liu, L. Feng, G. Z. Hu, J. Luo and X. J. Liu, *Int. J. Hydrogen Energy*, 2024, **53**, 318–324.
44 R. Zhou, X. Fan, X. X. Ke, J. Xu, X. Zhao, L. Jia, B. B. Pan, N. Han, L. X. Li, J. Luo, H. P. Lin and Y. G. Li, *Nano Lett.*, 2021, **21**, 4092–4098.
45 A. Rodríguez-Gómez, E. Lepre, L. Sánchez-Silva, N. López-Salas and A. R. Osa, *J. Energy Chem.*, 2022, **66**, 168–180.
46 Y. Zhang, S. Li, C. Sun, P. Wang, Y. Yang, D. Yi, X. Wang and J. Yao, *ACS Catal.*, 2022, **12**, 9201–9212.
47 B. Sun, Y. C. Jiang, Q. L. Hong, X. Liu, F. M. Li, D. S. Li, Y. Yang and Y. Chen, *J. Energy Chem.*, 2023, **85**, 481–489.
48 S. Mine, M. Takao, T. Yamaguchi, T. Toyao, Z. Maeno, S. M. A. H. Siddiki, S. Takakusagi, Ki Shimizu and I. Takigawa, *ChemCatChem*, 2021, **13**, 3636–3647.
49 K. L. Wang, P. C. Liu, M. Z. Wang, T. R. Wei, J. T. Lu, X. L. Zhao, Z. Y. Jiang, Z. M. Yuan, X. J. Liu and J. He, *Chin. Chem. Lett.*, 2025, **36**, 110532.
50 X. Y. Zhang, R. R. Wei, M. Yan, X. L. Wang, X. W. Wei, Y. L. Wang, L. Wang, J. M. Zhang and S. L. Yin, *Adv. Funct. Mater.*, 2024, 2401796.
51 Z. J. Li, X. Jiang, X. R. Wang, J. R. Hu, Y. Y. Liu, G. T. Fu and Y. W. Tang, *Appl. Catal., B*, 2020, **277**, 119135.
52 X. Li, Y. M. Liu, J. J. Zhang, B. Yan, C. Q. Jin, J. J. Dou, M. Y. Li, X. H. Feng and G. Liu, *Chem. Mater.*, 2022, **34**, 1385–1391.
53 J. Wang, A. Zhang, W. X. Niu, G. G. Liu, X. C. Zhou, L. X. Wang, X. Z. Liu, L. J. Li, Z. J. Li, L. Zhai, Q. Yang, B. Huang, Q. B. Wa, Q. B. Yun, H. F. Cheng, Y. Y. Ge, J. T. Huang, Z. N. Hu, B. Chen, Q. Y. Zhang, Z. X. Fan, L. Gu and H. Zhang, *Adv. Funct. Mater.*, 2024, 2405073.
54 B. Yang, W. Q. Zhang, S. L. Hu, C. Z. Liu, X. Q. Wang, Y. J. Fan, Z. Jiang, J. Yang and W. Chen, *J. Colloid Interface Sci.*, 2021, **600**, 503–512.
55 R. X. Feng, D. Li, H. Z. Yang, C. Y. Li, Y. X. Zhao, G. I. N. Waterhouse, L. Shang and T. R. Zhang, *Adv. Mater.*, 2024, **36**, 2309251.
56 Y. Liu, Y. C. He, D. D. Ma, X. T. Wu and Q. L. Zhu, *J. Colloid Interface Sci.*, 2023, **640**, 423–433.
57 Y. M. Zhu, J. L. Wei, J. Wu, R. Chen, P. Tsiakaras and S. B. Yin, *J. Colloid Interface Sci.*, 2024, **673**, 301–311.
58 Y. M. Liu, B. Q. Miao, H. Y. Yang, X. Ai, T. J. Wang, F. Shi, P. Chen and Y. Chen, *Adv. Funct. Mater.*, 2024, **34**, 2402485.
59 K. Chen, J. Q. Xiang, Y. Guo, X. J. Liu, X. G. Li and K. Chu, *Nano Lett.*, 2024, **24**, 541–548.